Bounding linear rainfall-runoff models with fractional derivatives applied to a barren catchment of the Jordan Rift Valley

Koichi Unami[a,1], Rasha M Fadhil[b], Osama Mohawesh[c]

[a] *Graduate School of Agriculture, Kyoto University, Kyoto 606-8502, Japan*

[b] *College of Engineering, University of Mosul, Mosul, Iraq*

[c] *Faculty of Agriculture, Mutah University, Karak 61710, Jordan*

Abstract

A new concept is developed to mathematically understand the dynamics of the rainfall-runoff events in a barren catchment of the Jordan Rift Valley. Time series data of rainfall and runoff have been acquired at an observation point in the catchment. Due to the extreme arid environment, water current as the runoff from the catchment is ephemeral, and the rainfall-runoff events are clearly distinguishable from each other. Firstly, a pair of linear autoregressive models with exogenous input (ARX models) is identified to tightly bound each runoff time series using the simplex method of linear programming. The exogenous input part is compatible with the conventional unit hydrograph method, while the autoregressive part is regarded as a discretized differential operator of fractional orders. Then, a linear fractional differential equation is determined to approximate each linear ARX model, which restricts the perturbation of the actual causal relationship between rainfall intensity and runoff discharge. The resulting lower and upper bounding rainfall-runoff models with fractional derivatives are examined in the system-theoretic framework. Finally, a nominal model from which actual nonlinear and stochastic phenomena perturb is arranged to envelope the all upper bounding rainfall-runoff models in the frequency domain, leading to the formulation of a challenging

[1] Corresponding author. *E-mail address:* unami.koichi.6v@kyoto-u.ac.jp *Phone:* +81-75-753-6161 (K. Unami)

fractional optimal control problem involving stochastic processes.

Keywords: Rainfall-runoff model, Jordan Rift Valley, ARX model, Linear programming, Fractional calculus, Transfer function

1. Introduction

One of the most known challenges in hydrology is to model dynamic behaviour of rainfall-runoff processes, whose input-output relationships are inherently nonlinear and stochastic. To merely simulate the phenomena, advanced technologies in these decades might be sufficient. Artificial neural network model approach (Furundzic, 1998; Hsu et al., 1995), fuzzy logic-based approach (Lohani et al., 2011), and physically-based spatially-distributed model approach (Deb et al., 2019; Emmanuel et al., 2015) are good examples. However, developing an appropriate hydrological model is not an easy task when attempting to represent dynamic causality based on time series data with a finite sampling interval, so that the model is applicable to practical problems of risk assessment or water resources management. So far, the authors have used the zero-reverting Ornstein–Uhlenbeck process for drought risk assessment (Sharifi et al., 2016), the Langevin equation for water flow index in irrigation water management (Unami and Mohawesh, 2018), and WGEN (Richardson and Wright, 1984) for optimal reservoir operation with a continuous state variable (Fadhil, 2018). The Langevin equation can be utilized for hydrological extreme value analysis as well (Rosmann and Dominguez, 2018). In contrast to these stochastic models, linear models have advantages of utilizing system-theoretic frameworks (Chang et al., 2019; Goswami et al., 2005; Karlsson and Yakowitz, 1987), especially when they are regarded as nominal models from which actual nonlinear and/or stochastic phenomena perturb. A primitive transfer function model of first order coupled with an estimation of error bounds has been proposed for rainfall-runoff processes in the first author's earlier work (Unami and Kawachi, 2005). Here, we consider linear autoregressive models with exogenous input (ARX models), which comprehend the conventional unit hydrograph method and autoregressive models, as well as their continuous time counterparts expressed as fractional differential equations.

ARX models applied to rainfall-runoff processes forecast the runoff discharges one sampling time ahead on the basis of linear combinations of the readily available values of hydrological variables (Osman et al., 2019). Conventional techniques have been developed to determine regression coefficients achieving the best fitting between model outputs and observations in the sense of least squares (Box et al., 1994). Other criteria such as absolute error and coefficient of efficiency are widely used for ad hoc evaluation of model performance (Cheng et al., 2017). A more rigorous but not well understood approach is to search a set of regression coefficients yielding envelope to tightly bound observed time series data in the sense of least absolute error. This can be achieved with the common simplex method of linear programming (LP) (Vedula and Mujumdar, 2005) when the rainfall-runoff event is of finite length in time, without necessitating any complex calibration procedure such as Duan et al. (1992), Duan et al. (2006), or Gautam and Holz (2001).

It is also not well known that a continuous time counterpart of a linear ARX model is expressed in the form of a linear differential equation including terms of fractional derivatives (Spolia et al., 1980), which well reproduce the effect of hysteresis, or memory effect, as in the autoregressive part. Differential equations including terms of fractional derivatives have been employed for modelling different practical phenomena such as population dynamics (Bushnaq et al., 2018a), HIV/AIDS infection (Bushnaq et al., 2018b), and infiltration of water into soil (Fernández-Pato et al., 2018). A rainfall-runoff model with a fractional differential equation has been developed in the pioneering work of Guinot et al. (2015).

This paper presents a constructive approach to obtaining linear rainfall-runoff models with fractional derivatives from time series data acquired at an observation point in a barren catchment in the Lisan Peninsula of the Dead Sea at the bottom of the Jordan Rift Valley. Water current in the catchment is ephemeral due to the extreme arid environment, and the rainfall-runoff events are clearly distinguishable from each other. Complexity of the rainfall-runoff processes there stems from the presence of salt layers, overhanging cliffs, caverns, and sinkholes in the karst system (Closson et al., 2007), and the fractional differential equations are expected to model pathological phenomena with memory effect there such as hysteresis in soil moisture retention, non-Darcy flows in the karst system, and discontinuous surface flows which may be of zero-depth. Time series data with a sampling interval of 1 minute have been successfully acquired for thirteen (13) rainfall-runoff events of finite lengths ranging from 69 minutes to 718 minutes, occurred in five (5) rainy seasons. This minuteness of available information makes it difficult to follow the innocent approaches based on the conventional statistical hydrology, which has been useful if the spatio-temporal scale is large; there are successful case studies in arid and semi-arid regions such as Ajami et al. (2017) on multiple stations across Australia, Bai et al. (2014) on headstreams of Tarim River in Northwest China, and Bahmed and Bouzid-Lagha (2020) on an Algerian ephemeral stream. Thus, we introduce the approach to consider perturbation from a linear nominal model. Firstly, the bounding linear ARX models are obtained for each rainfall-runoff event, using the simplex method of LP minimizing the mean absolute error. Then, their continuous time counterparts are established as fractional differential equations. Finally, the bounding linear rainfall-runoff models with fractional derivatives are examined in the system-theoretic framework, where the response of the runoff discharge to the rainfall intensity is evaluated in the frequency domain (Jarad and Abdeljawad, 2018). Furthermore, a nominal model from which actual phenomena perturb is arranged. Such models representing dynamic causality in hydrological phenomena are definitely useful for design and operation of water control structures. There has been significant development in the research field of deterministic fractional optimal control problems to obtain the Pontryagin maximum principles (Agrawal, 2004; Kamocki, 2014a; Kamocki, 2014b; Kamocki and Majewski, 2015), however, the approach developed here leads to a challenging fractional optimal control problem involving stochastic processes.

2. Materials and methods

2.1 Study site

The Jordan Rift Valley refers to the depression below the sea level extending over the range of latitudes 30-33 N and longitudes 35-36 E, including Lake Tiberias to the north and the Dead Sea in the middle, surrounded by Jordanian Highlands and Judaean Mountains (Van Afferden et al., 2010). Figure 1 shows the topography of the region including the Jordan Rift Valley, depicted with the SRTM digital elevation data (Farr et al., 2007). Situated in the lee side of the Judean mountains with a westerly descending dry and hot wind, the environment of the Jordan Rift Valley is subject to an arid climate (Tarawneh and Kadıoğlu, 2003). Hadadin and Tarawneh (2007) reported that the water level of the Dead Sea was significantly receding at a rate of about 1 m per year. This receding rate is almost constant during these decades, and the water level is 431 m below the sea level as of 2020. Currently, the dried-up southern part of the Dead Sea is mainly used for salt evaporation ponds to produce potash, while the other dried-up land may be used as farmlands if the constraints of aridity and salinity are solved (Unami et al., 2015). Figure 1 also shows the location of the study site in the Lisan Peninsula of the Dead Sea, and Figure 2 provides a close-up view, where the position of the observation point (red dot), delineation of its catchment area (yellow line), and the position of an auxiliary raingauge (green dot) are indicated. The catchment area is a barren land of 1.12 km^2, and hydraulic structures have been constructed at the outlet in order to collect ephemeral water current: flash floods are harvested at a gutter cutting across a 16 m wide valley bottom and then guided to a reservoir through a conveyance channel of 60 m long (Unami and Mohawesh, 2018). The conveyance channel is equipped with a spillway to release excess backwater from the reservoir. Figure 3 is a photo of the catchment area near the outlet including the gutter of the flash flood harvesting structure. The salt layers have been eroded to form the overhanging cliffs and caverns, as can be seen in the photo. Substantial rainfall-runoff events occur only during the rainy season from October to May, sometimes causing disastrous floods. The harvested water of flash floods is desalinated and used for irrigation of perennial crops (Unami et al., 2020). Table 1 summarizes the basic meteorological data obtained at the study site from the observation detailed in the next subsection, in terms of the rainfall depth D (mm) for each month from October 2014 through July 2019, the total rainfall depth for each water year, the monthly and annual maximum, mean, and minimum values of air temperature T (℃).

Figure 1: The topography of the region including the Jordan Rift Valley and the location of the study site.

Figure 2: Close-up view of the study site in the Lisan Peninsula of the Dead Sea.

Figure 3: Photo of the catchment area near the outlet with the gutter.

Table 1: Basic meteorological data of rainfall depth D (mm) and air temperature T (℃) obtained at the study site for each water year.

2.2 Data collection of rainfall and runoff time series

As shown in the photos of Figure 4, the observation point has been set up over the conveyance channel of $B = 1.6$ m wide rectangular cross-section, at the coordinates 31 15 33.2 N 35 29 20.2 E which falls on the point 2.4 m upstream from the downstream end, operating with a Campbell data logger connected to a VAISALA multi-weather sensor and a Campbell water level sensor. The data logging interval is normally 10 minutes, but it switches to 1 minute if the rainfall depth in the last 10 minutes is equal to or greater than 0.2 mm. If there is no rainfall for 12 hours, then the logging interval returns back to 10 minutes. This observation system has been operating since late September of 2014. As a result of numerical experiment based on the two-dimensional shallow water equations (Sharifi et al., 2015), a functional relationship between the observed water depth h (m) and runoff discharge Q (m^3/s) is determined as

$$Q = 3.4996 A R^{0.26999} \tag{1}$$

where $A = Bh$ is the cross-sectional area, and $R = A/(B + 2h)$ is the hydraulic radius. The auxiliary raingauge is of a tipping-bucket type and located at the coordinates 31 15 41.2 N 35 29 39.5 E, 566 m apart from the observation point.

Figure 4: Measurement system at the observation point

2.3 Linear ARX models and parameter identification

The observed rainfall-runoff events are ephemeral and clearly distinguishable from each other. For each rainfall-runoff event, we consider discrete time series consisting of rainfall intensity r_t (constant from the time $t-1$ until the time t) and runoff discharge Q_t (at the time t). A linear ARX model with the orders n_r and n_Q is written as

$$\hat{Q}_{t+1} = \sum_{k=0}^{k<n_r} r_{t-k} x_k + \sum_{k=0}^{k<n_Q} Q_{t-k} x_{n_r+k} \tag{2}$$

where x_t are the regression coefficients, to estimate the runoff discharge $\hat{Q}_{t+1}$ at the time $t+1$. It is assumed that $r_t = 0$ and $Q_t = 0$ if $t < 0$ or $t \geq N$, where the length N of the rainfall-runoff event is finite. The regression coefficients x_t for all t, as well as the linear ARX model (2) itself, are referred to as lower bounding and upper bounding if $Q_t \geq \hat{Q}_t$ and $Q_t \leq \hat{Q}_t$, respectively. The lower and upper bounding linear ARX models restrict the perturbation of the actual causal relationship between r_t and Q_t. A standard LP problem is formulated to identify the best set of lower bounding regression coefficients x_t^L minimizing the objective function $\sum_{t=0}^{t<N} \left(Q_t - \hat{Q}_t \right)$, which is expressed in canonical form as

$$\text{Maximize } \mathbf{c}^T \mathbf{x}^L \text{, subject to } A\mathbf{x}^L \leq \mathbf{b} \text{ and } \mathbf{x}^L \geq \mathbf{0} \tag{3}$$

where $\mathbf{x}^L$ is a $n_r + n_Q$-dimensional vector whose tth entry is x_t^L, and

$$\left[\begin{array}{c|c} \mathbf{c}^T & 0 \\ \hline A & \mathbf{b} \end{array} \right] = \left[\begin{array}{c|c} \left[\sum_{t=0}^{t<N} r_{t-j} \;\middle|\; \sum_{t=0}^{t<N} Q_{t-j} \right] & 0 \\ \hline \left[r_{i-j} \;\middle|\; Q_{i-j} \right] & \left[Q_{i+1} \right] \end{array} \right]. \tag{4}$$

While, the best set of upper bounding regression coefficients x_t^U maximizing the objective function $\sum_{t=0}^{t<N} \left(Q_t - \hat{Q}_t \right)$ solves the LP problem

$$\text{Minimize } \mathbf{c}^T \mathbf{x}^U \text{, subject to } A\mathbf{x}^U \geq \mathbf{b} \text{ and } \mathbf{x}^U \geq \mathbf{0} \tag{5}$$

where $\mathbf{x}^U$ is a $n_r + n_Q$-dimensional vector whose tth entry is x_t^U, which is indeed the dual of (3). Then, the simplex algorithm is applicable to solving both of (3) and (5). Conversely, the approach here is not transferable to the rainfall-runoff processes with permanent streamflows as the dimension of the LP problem becomes infinite.

2.4 Fractional differential equations to approximate linear ARX models

A continuous time counterpart of a linear ARX model is expressed in the form of a linear differential equation including terms of fractional derivatives, which well reproduce the effect of hysteresis as in the autoregressive part. The lower and upper bounding linear ARX models are represented as

$$Q_{t+1} - \sum_{k=0}^{k<n_Q} Q_{t-k} x^L_{n_r+k} \ge \sum_{k=0}^{k<n_r} r_{t-k} x^L_k \tag{6}$$

and

$$Q_{t+1} - \sum_{k=0}^{k<n_Q} Q_{t-k} x^U_{n_r+k} \le \sum_{k=0}^{k<n_r} r_{t-k} x^U_k \ , \tag{7}$$

respectively. Discretized fractional derivatives are employed for approximating the left hand sides of (6) and (7). According to Oldham and Spanier (1974), the α-th fractional derivatives of Q as a smooth function of the time *t*, whose unit is taken as the sampling interval of the discrete time series data, are approximated as

$$\frac{d^\alpha Q}{dt^\alpha} \approx \frac{1}{\Gamma(2-\alpha)} \left[\sum_{k=0}^{k<n_Q} \left(Q_{t+1-k} - Q_{t-k}\right)\left(\left(k+1\right)^{1-\alpha} - k^{1-\alpha}\right) + \frac{1-\alpha}{n_Q^\alpha} Q_{t+1-n_Q} \right] = \sum_{k=0}^{k\le n_Q} c_{\alpha,k} Q_{t+1-k} \tag{8}$$

for $0 \le \alpha < 1$ and

$$\frac{dQ}{dt} \approx \frac{Q_{t+1} - Q_{t+1-n_Q}}{n_Q} = \sum_{k=0}^{k\le n_Q} c_{1,k} Q_{t+1-k} \ , \tag{9}$$

which are linear combinations of Q_{t+1-k}. Here, the fractional orders are chosen as $\alpha = k/n_Q$ for $k = 0, \cdots, n_Q$, so that the left hand sides of (6) and (7) are consistently approximated as

$$\sum_{k=0}^{k\le n_Q} a^B_k \frac{d^{k/n_Q} Q}{dt^{k/n_Q}} \approx Q_{t+1} - \sum_{k=0}^{k<n_Q} Q_{t-k} x^B_{n_r+k} \tag{10}$$

where B represents L and U, respectively, with

$$M\mathbf{a}^B = \begin{pmatrix} 1 \\ -x_{n_r} \\ \vdots \\ -x_{n_r+n_Q-1} \end{pmatrix} \tag{11}$$

where M is the $(n_Q+1)\times(n_Q+1)$ matrix whose (i,j)th entry is $c_{j/n_Q,i}$, $\mathbf{a}^B$ is the (n_Q+1)-dimensional vector whose kth entry is a_k^B. Then, bounding linear rainfall-runoff models with fractional derivatives are represented as transfer functions

$$P^B(s) = \frac{1-\exp(-s)}{s} \frac{\sum_{k=0}^{k<n_r} x_k^B \exp(-ks)}{\sum_{k=0}^{k\le n_Q} a_k^B s^{k/n_Q}} \tag{12}$$

where s is the complex frequency in the Laplace transform.

3. Results and discussions

Numerical computations in this section are implemented with the units (min) for the time, (mm/hour) for the rainfall intensity r, and (L/s) for the runoff discharge Q. However, the gains of transfer functions are converted to runoff coefficients (%) for presentation in Figures 7, 8, and 9.

3.1 Acquired data sets

Time series data with the sampling interval of 1 minute has been successfully acquired for thirteen rainfall-runoff events with total runoff volume more than 100 m^3, as shown in Table 2 summarizing the starting time, the ending time, the length *N*, the total rainfall depth D^o at the observation point, the total rainfall depth D^a at the auxiliary raingauge, the total runoff volume V, the maximum runoff discharge $Q_{\max}$, and the bulk runoff coefficient C for each rainfall-runoff event, whose date of occurrence is used as the event ID number. There were other 2 significant rainfall-runoff events on April 12, 2015 and on February 22, 2016, but the observation system failed to record them due to technical problems. The difference between the two total rainfall depths in each event implicates spatial variability of rainfall distribution within the catchment area.

Table 2: Observed rainfall-runoff events with total runoff volume more than 100 m^3.

3.2 Identification of model parameters

The order of the linear ARX model is consistently set as $n_r = N$ for the exogenous part, while two cases of $n_Q = 1$ and $n_Q = 2$ are examined for the autoregressive part. There is no technical difficulty in solving the LP problems for cases of $n_Q > 2$, but this study focuses on those fundamental two cases. According to the methods described in the subsections 2.3 and 2.4, the model parameters are identified. For all events and for both cases of $n_Q = 1$ and $n_Q = 2$, all $x^L_{n_r+k}$ ($0 \le k < n_Q$) become zero, implying that the lower bounding models are of unit hydrograph (UH) type without autoregressive part. The values of $x^U_{n_r+k}$ and a^U_α are shown in Table 3. The events 09JAN2016, 13APR2016, 17FEB2018, and 07FEB2019 yield the upper bounding models of UH type, where $x^U_{n_r+k} = 0$ ($0 \le k < n_Q$). Positive values of $x^U_{n_r}$ appear in the events 26OCT2015, 26APR2018, 25MAR2019a, and 25MAR2019b, where $x^U_{n_r}$ for the case of $n_Q = 2$ is identical to that for the case of $n_Q = 1$ and $x^U_{n_r+1} = 0$. Though the ARX models are the same, the approximating fractional differential equations are different between the cases of $n_Q = 1$ and $n_Q = 2$. This type shall be referred to as ARX-1 type. Substantial differences can be seen between the cases of $n_Q = 1$ and $n_Q = 2$ for the events 12DEC2014, 11JAN2015, 14JAN2015, 16FEB2017, and 10MAR2017, which are categorized as ARX-2 type. However, the event 14JAN2015 is significantly different from the others, as the upper bounding models are unstable ($x^U_{n_r} > 1$ and then $a^U_0 < 0$) for the case of $n_Q = 1$ but they become stable for the case of $n_Q = 2$.

Table 3: Identified parameters of upper bounding models.

3.3 Evaluation of the models

This subsection contains results and discussions overviewed as follows. Firstly, performances of the linear ARX models are evaluated in terms the errors between the observed runoff discharges Q_t and the estimated runoff discharges $\hat{Q}_t$ as in (2), using different five indices. Then, several representative events are examined in the time domain, before focusing on the terms of fractional derivatives in the frequency domain. Finally, the nominal model is defined to deal with all the events as its perturbations. Utility of the nominal model is addressed in the context of the control theory in fractional calculus.

For evaluation of performances of the linear ARX models, the five indices are defined as

$$E_1 = \frac{1}{N}\sum_{t=0}^{t<N}\left|Q_t - \hat{Q}_t\right|, \tag{13}$$

$$E_2 = \frac{1}{N}\sum_{t=0}^{t<N}\left|Q_t - \hat{Q}_t\right|^2, \tag{14}$$

$$E_{\infty} = \max_{0 \le t < N} \left| Q_t - \hat{Q}_t \right|, \tag{15}$$

$$E_{\mathrm{TV}} = \sum_{t=0}^{t<N-1} \left| Q_{t+1} - Q_t - \hat{Q}_{t+1} + \hat{Q}_t \right|, \tag{16}$$

and

$$\mathrm{NSE} = 1 - \frac{\sum_{t=0}^{t<N} \left| Q_t - \hat{Q}_t \right|^2}{\sum_{t=0}^{t<N} \left| Q_t - \bar{Q}_t \right|^2} \tag{17}$$

where $\bar{Q}_t$ is the mean of the observed runoff discharges Q_t. The index E_1 is the mean absolute error, which is indeed minimized in the LP problems. The indices E_2 and E_{∞} are the mean squared error and the maximum absolute error, respectively. The index E_{TV} represents the error of total variation, which is more appropriate than E_2 and E_{∞} when dealing with time series in broader sense (Unami et al., 2019). The index NSE is the Nash–Sutcliffe Efficiency coefficient, which is the most utilized index in hydrological applications involving correlations between observed and estimated values (Biondi et al., 2012). Table 4 shows the values of the indices for the upper bounding linear ARX models. Table 5 shows the values of the indices for the lower bounding linear ARX models, as well as changes in the values of Table 4 from the case of $n_Q = 1$ to the case of $n_Q = 2$. It is trivial that there is no change in all the indices by n_Q for the events of UH type and ARX-1 type and that E_1-values do not increase when n_Q increases from 1 to 2 for the events of ARX-2 type, as can be confirmed in Table 5. Indeed, the E_1-values decrease for all the events of ARX-2 except 14JAN2015, where the E_1-values does not change. No definite effect of n_Q can be found on the E_2-values and on the E_{∞}-values. It should be noted that the E_{TV}-values decrease for all the events of ARX-2. The NSE-values are close to unity for the upper bounding linear ARX models, indicating high correlations between the observed runoff discharges and the estimates, but diverse for the lower bounding linear ARX models. The event 09JAN2016 has an exceptional linear property such that the NSE-values are high both for the lower and the upper bounding linear ARX models. The NSE-values do not indicate an explicit dependency on the types.

Table 4: Performance indices of the upper bounding linear ARX models.

Table 5: Performance indices of the lower bounding linear ARX models and changes in performance indices of the upper bounding linear ARX models by increasing n_Q from 1 to 2.

For the sake of brevity, 13APR2016 of UH type, 26APR2018 of ARX-1 type, 10MAR2017 of ARX-2 type changing E_1-values the most, 16FEB2017 of ARX-2 type changing E_{TV}-values the most, and 14JAN2015 of ARX-2 type stabilized by $n_Q = 2$ are chosen as representative events for discussion. In Figure 5, rainfall intensity (dark blue bar), observed runoff discharge (red line), and the region of runoff discharge bounded by the estimates of the two linear ARX models with $n_Q = 1$ (green area) are depicted in the time domain for the events 13APR2016, 26APR2018, 10MAR2017, 16FEB2017, and 14JAN2015. Similarly, Figure 6 shows the observed time series and the bounded region with $n_Q = 2$ for the events 10MAR2017, 16FEB2017, and 14JAN2015, which are of ARX-2 type. The runoff discharge of the event 13APR2016 was extraordinarily large, but the linear ARX models are of UH type implying straightforward linear input-output relationship between rainfall and runoff. There are many peaks of rainfall and runoff in the event 26APR2018 of ARX-1 type, where linearity is still noticeable. There are two evident spikes of rainfall intensity with similar wave forms in the event 10MAR2017 of ARX-2 type, but the response of runoff is rather irregular. Such nonlinearity is more dominant in the events 16FEB2017 and 14JAN2015. Differences between the bounded regions with $n_Q = 1$ and $n_Q = 2$ are minor in the events 10MAR2017 and 16FEB2017 and almost invisible in the event 14JAN2015, though the linear ARX models are substantially different. The lower bounding linear ARX model for the event 16FEB2017 is almost vanishing.

Figure 5: Rainfall intensity, observed runoff discharge, and the region of runoff discharge bounded by the estimates of the two linear ARX models with $n_Q = 1$ for the events 13APR2016, 26APR2018, 10MAR2017, 16FEB2017, and 14JAN2015.

Figure 6: Rainfall intensity, observed runoff discharge, and the region of runoff discharge bounded by the estimates of the two linear ARX models with $n_Q = 2$ for the events 10MAR2017, 16FEB2017, and 14JAN2015.

Comparisons are made among the lower and the upper bounding linear rainfall-runoff models of $n_Q = 1$ and $n_Q = 2$ which may include terms of fractional derivatives. Figure 7 shows the gains $\left| P^B\left(\sqrt{-1}\omega\right) \right|$ of the transfer functions (12) for the representative events 13APR2016, 26APR2018, 10MAR2017, 16FEB2017, and 14JAN2015, for the frequency ω between $2^{-30}\pi$ and $2^{10}\pi$. The bulk runoff coefficient C in Table 2 is regarded as the bulk gain and thus depicted in these figures as well. There is no difference between the cases of $n_Q = 1$ and $n_Q = 2$ for the event 13APR2016 of UH type, including no fractional derivative. It is indefinite whether the gains of the upper bounding linear rainfall-runoff models increase or decrease when n_Q increases from 1 to 2 for the events of ARX-1 type and ARX-2 type. However, the unreasonably high gains larger than the bulk runoff coefficient for the event 14JAN2015 are resolved by the stabilization with $n_Q = 2$. It is also remarked that approximating linear ARX models of ARX-1 type with fractional differential equation with the three orders 0, $1/2$, and 1 makes (11) ill-conditioned. Therefore, we opt for the case of $n_Q = 1$ to approximate linear ARX models of ARX-1 type.

Figure 7: Comparison among the lower and the upper bounding linear rainfall-runoff models of $n_Q = 1$ and $n_Q = 2$ for the events 13APR2016, 26APR2018, 10MAR2017, 16FEB2017, and 14JAN2015.

The gains of the bounding linear rainfall-runoff models with fractional derivatives for all events are summarized in Figures 8 and 9. Terms of fractional derivatives indeed appear in the upper bounding models of ARX-2 type only. The event 13APR2016 is extraordinary because the gains of both the lower and the upper bounding models are large even in higher frequency domains. The other events of large gains of the upper bounding models are 26APR2018, 16FEB2017, 11JAN2015, and 26OCT2015, but the gains of their lower bounding models are very small. The gains of the upper bounding models for the events of ARX-2 type attain notable peaks at the frequency ω between $2^{-15}\pi$ and $2^{-5}\pi$, due to the terms of fractional derivatives. It can be seen that each of the upper bounding models functions as a low-pass filter that diminishes fluctuations of high frequencies in the rainfall-runoff process. Now, in order to encompass all the events, we consider envelopes to bound the gains of the upper bounding models for all the events from above. The infimums of the gains of the lower bounding models for all the events are so small that envelopes for them are not discussed. A transfer function model attaining such an envelope is expected to serve as a nominal model in stochastic problems such as flood risk assessment or real time operation of water harvesting facilities, particularly in arid environments. An ad hoc example of such a transfer function $\bar{P}(s)$ including a term of fractional order $1/2$ is given by

$$\bar{P}(s) = \frac{1}{0.025 + 0.020 s^{1/2} - 0.020 s}, \tag{18}$$

and its gains are plotted in Figure 9 as well. The actual transfer function $P^{B}(s)$ of each upper bounding rainfall-runoff model is thus represented as

$$P^{B}(s) = W(s)\bar{P}(s) \tag{19}$$

where $W(s)$ is a transfer function of the perturbation whose maximum absolute value of gain is less than unity. The validity of $\bar{P}(s)$ as the nominal model is the upper bounding properties, which are tested by operating the discrete-time domain counterpart of $\bar{P}(s)$ on the time series data of rainfall in each of the events. For this purpose of validation, the approximation (8) of the fractional derivative is performed with $n_Q = N$ and $n_r = 1$, in contrast to the linear ARX models' construction where $n_Q = 1$ or 2 and $n_r = N$. Figure 10 compares the observed values with the values that the nominal model generates in terms of the metrics *V*, $Q_{\max}$, the total variation $\mathrm{TV}[Q] = \sum_{t=0}^{t<N-1} |Q_{t+1} - Q_t|$ of the runoff discharge, and the maximum variation $\mathrm{MV}[Q] = \max_{0 \le t < N-1} |Q_{t+1} - Q_t|$ of the runoff discharge, confirming that the upper bounding properties are achieved in all the metrics. The gain of $\bar{P}(s)$ at $\omega = 0$, which is equal to 40 and is equivalent to 12.86 % in terms of runoff coefficient, represents the runoff coefficient for a constant rainfall intensity r. This value, which is 32.9 % larger than the historical maximum bulk runoff coefficient of 9.68 % observed in the event 13APR2016, can be utilized for determining design flood discharges at analogous locations for specified rainfall intensities. As the gain of $\bar{P}(s)$ substantially decreases when $\omega > \pi$, rainfall intensities of sub-minute durations are considered insignificant. The historical maximum rainfall intensity in 1 minute at the study site is 116.4 (mm/hour) observed in the event 17FEB2018, and the design flood discharge according to that method becomes 4656 (L/s), which would be more reasonable than the historical maximum $Q_{\max}$ = 1816 (L/s), observed in the event 13APR2016, multiplied by an arbitrary safety ratio.

Figure 8: Gains of the lower bounding linear rainfall-runoff models for all events.

Figure 9: Gains of the upper bounding linear rainfall-runoff models with fractional derivatives for all events and an ad hoc example of their envelopes.

Figure 10: Validation of the nominal model in terms of the metrics V, $Q_{\max}$, $\mathrm{TV}[Q]$, and $\mathrm{MV}[Q]$.

Further utility of the nominal model is in the application of the control theory in fractional calculus. The dynamical system corresponding to the transfer function $\bar{P}(s)$ of (18) is

$$\frac{\mathrm{d}^{1/2}}{\mathrm{d}t^{1/2}}\begin{pmatrix} y \\ z \end{pmatrix} = \begin{pmatrix} 0.00 & 1.00 \\ 1.25 & 1.00 \end{pmatrix}\begin{pmatrix} y \\ z \end{pmatrix} + \begin{pmatrix} 0 \\ -50.0r \end{pmatrix} \tag{20}$$

where y and z are the state variables. The initial value problem for (20) with the initial condition $y = z = 0$ at $t = 0$ has a unique solution for the rainfall intensity r being a summable function in a finite time domain, according to Theorem 4.1 of Idczak and Kamocki (2011), which gives an explicit form of the unique solution and verifies the stability of (20) as well. With (19), the runoff discharge $Q(t)$ in the time domain is constrained as

$$Q(t) \le \int_0^t w(\tau)\, y(t-\tau)\, \mathrm{d}\tau \tag{21}$$

where $w(t)$ is the inverse Laplace transform of $W(s)$. Therefore, it is well-defined to formulate a fractional optimal control problem for real time operation of a water harvesting facility as below.

Problem: *Let* $u(t)$ *be the discharge of flow being harvested from a flash flood at the time* t. *The harvested flow is assumed to be immediately stored in a reservoir; the storage volume of the reservoir at the time* t, *which is denoted by* $S(t)$, *is related to* $u(t)$ *as*

$$S(t) = S(0) + \int_0^t u(\tau)\,\mathrm{d}\tau . \tag{22}$$

The rainfall intensity $r = r(t)$ *is assumed to be a càdlàg stochastic process whose probability law is provided. The transfer function* $W(s)$ *of the perturbation is assumed to be specified so that its maximum absolute value of gain becomes less than unity. The initial time* $t = 0$ *is set as the time of* $Q = 0$ *as well as* $r > 0$ *but also* $\lim_{t \to -0} r(t) = 0$. *Let* T *be the first exit time such that*

$$T = \inf \left\{ t > 0 \,\middle|\, r(t) = 0 \text{ and } Q(t) = 0 \right\} . \tag{23}$$

The discharge $u(t)$ *is considered as the control variable constrained in a set of admissible control. The optimal control problem is to find*

$$u(t) = u\big(t, r(t), Q(t), S(t)\big), \tag{24}$$

as a function of the four variables, so as to maximize the functional

$$J^u\big(t, r(t), Q(t), S(t)\big) = \mathrm{E}\big[S(T)\big], \tag{25}$$

which is the expectation of the storage volume in the reservoir when the rainfall-runoff flood event is over.

This problem statement is quite general for ephemeral flows as the probability that the first exit time T is finite is equal to 1. However, the Pontryagin maximum principles obtained so far are not applicable to this stochastic problem, which shall be tackled in future studies.

4. Conclusions

A general methodology to construct bounding linear rainfall-runoff models with fractional order derivatives was presented and applied to the time series data acquired at the observation point in the barren catchment of the Jordan Rift valley. The short sampling interval of 1 minute motivated us to study conceptual discrete time models as well as their continuous time counterparts.

The ARX models representing dynamic causality between rainfall and runoff comprehend the conventional unit hydrograph method and autoregressive method, and an advantage of the bounding linear ARX models is that the parameter identification process is complete with the simplex algorithm of LP if the length of each rainfall-runoff event is finite. Innovation in the methodology is the introduction of fractional derivatives into continuous time counterparts of the linear ARX models, and that approximation procedure is applicable to perennial rainfall-runoff processes as well.

The bounding linear rainfall-runoff models were identified for the thirteen events and evaluated. However, only the terms of fractional order $1/2$ were considered. The models were categorized into the three types, according to the substantial fractional orders. The all lower bounding models are of UH type, and some of them are almost vanishing. The most significant effect of fractional derivatives is stabilization of the upper bounding model for the event 14JAN2015 of type ARX-2. As usual in the system-theoretic framework, the fractional order differential equations were regarded as input-output systems whose transfer functions were evaluated in terms of gains. Finally, the nominal model was arranged to estimate the design flood discharge and to formulate the fractional optimal control problem for real time operation of a water harvesting facility. Such applications of nominal models shall be disseminated to practical problems of risk assessment and water resources management in future studies, linked with research on stochastic fractional optimal control.

CRediT Author Statement

Koichi Unami: Methodology, Validation, Software, Data Curation, Writing - Original Draft, Writing - Review & Editing, Visualization, Supervision, Funding acquisition.

Rasha M. Fadhil: Conceptualization, Formal analysis, Investigation, Writing - Original Draft, Writing - Review & Editing.

Osama Mohawesh: Conceptualization, Resources, Writing - Review & Editing, Supervision, Project administration.

Declaration of Competing Interest

The authors declare that they have no known competing financial interests or personal relationships that could have appeared to influence the work reported in this paper.

Acknowledgments

This research is funded by grants-in-aid for scientific research No.26257415, No.16KT0018, and No.19KK0167 from the Japan Society for the Promotion of Science (JSPS).

References

Agrawal, O.P., 2004. A general formulation and solution scheme for fractional optimal control problems. Nonlinear Dynam, 38(1-4): 323-337.

https://doi.org/10.1007/s11071-004-3764-6

Ajami, H. et al., 2017. On the non-stationarity of hydrological response in anthropogenically unaffected catchments: an Australian perspective. Hydrol. Earth Syst. Sci., 21(1): 281-294. https://doi.org/10.5194/hess-21-281-2017

Bahmed, A.T., Bouzid-Lagha, S., 2020. Quantitative analysis and efficiency assessment of floodwater harvesting system in arid region: case of Touzouz ephemeral stream—Mzab Valley. Water Resour., 47: 54–64. https://doi.org/10.1134/S0097807820010029

Bai, Y.A., Xu, H.L., Ling, H.B., 2014. Drought-flood variation and its correlation with runoff in three headstreams of Tarim River, Xinjiang, China. Environ Earth Sci, 71(3): 1297-1309. https://doi.org/10.1007/s12665-013-2534-5

Biondi, D., Freni, G., Iacobellis, V., Mascaro, G., Montanari, A., 2012. Validation of hydrological models: Conceptual basis, methodological approaches and a proposal for a code of practice. Phys. Chem. Earth., 42-44: 70-76. https://doi.org/10.1016/j.pce.2011.07.037

Box, G.E.P., Jenkins, G.M., Reinsel, G.C., 1994. Time series analysis: forecasting and control. Prentice-Hall, New Jersey.

Bushnaq, S., Ali, S., Shah, K., Arif, M., 2018a. Exact solution to non-linear biological population model with fractional order. Therm. Sci., 22: S317-S327. https://doi.org/10.2298/TSCI171127035B

Bushnaq, S., Khan, S.A., Shah, K., Zaman, G., 2018b. Mathematical analysis of HIV/AIDS infection model with Caputo-Fabrizio fractional derivative. Cogent Math., 5(1): 1432521. https://doi.org/10.1080/23311835.2018.1432521

Chang, C.M., Yeh, H.D., Chuang, M.H., 2019. Spectral analysis of temporal variability of nonlinear and nonstationary rainfall-runoff processes. J. Hydrol., 575: 1301-1307. https://doi.org/10.1016/j.jhydrol.2019.05.086

Cheng, K.S., Lien, Y.T., Wu, Y.C., Su, Y.F., 2017. On the criteria of model performance evaluation for real-time flood forecasting. Stoch. Environ. Res. Risk Assess., 31(5): 1123-1146. https://doi.org/10.1007/s00477-016-1322-7

Closson, D., LaMoreaux, P.E., Abou Karaki, N., al-Fugha, H., 2007. Karst system developed in salt layers of the Lisan Peninsula, Dead Sea, Jordan. Environ. Geol., 52(1): 155-172. https://doi.org/10.1007/s00254-006-0469-9

Deb, P., Kiem, A.S., Willgoose, G., 2019. A linked surface water-groundwater modelling approach to more realistically simulate rainfall-runoff non-stationarity in semi-arid regions. J. Hydrol., 575: 273-291. https://doi.org/10.1016/j.jhydrol.2019.05.039

Duan, Q. et al., 2006. Model Parameter Estimation Experiment (MOPEX): An overview of science strategy and major results from the second and third workshops. J. Hydrol., 320(1-2): 3-17. https://doi.org/10.1016/j.jhydrol.2005.07.031

Duan, Q.Y., Sorooshian, S., Gupta, V., 1992. Effective and Efficient Global Optimization for Conceptual Rainfall-Runoff Models. Water Resour. Res., 28(4): 1015-1031. https://doi.org/10.1029/91wr02985

Emmanuel, I., Andrieu, H., Leblois, E., Janey, N., Payrastre, O., 2015. Influence of rainfall spatial variability on rainfall-runoff modelling: Benefit of a simulation approach? J. Hydrol., 531: 337-348. https://doi.org/10.1016/j.jhydrol.2015.04.058

Fadhil, R.M., 2018. Daily operation of Bukit Merah Reservoir with stochastic dynamic programming under the impact of climate change, Universiti Putra Malaysia, 220 pp.

Farr, T.G. et al., 2007. The shuttle radar topography mission. Rev. Geophys., 45(2): RG2004. https://doi.org/10.1029/2005RG000183

Fernández-Pato, J., Gracia, J.L., Garcia-Navarro, P., 2018. A fractional-order infiltration model to improve the simulation of rainfall/runoff in combination with a 2D shallow water model. J. Hydroinform., 20(4): 898-916. https://doi.org/10.2166/hydro.2018.145

Furundzic, D., 1998. Application example of neural networks for time series analysis: Rainfall-runoff modeling. Signal Process, 64(3): 383-396. https://doi.org/10.1016/S0165-1684(97)00203-X

Gautam, D.K., Holz, K.P., 2001. Rainfall-runoff modelling using adaptive neuro-fuzzy systems. J. Hydroinform., 3(1): 3-10. https://doi.org/10.2166/hydro.2001.0002

Goswami, M., O'Connor, K.M., Bhattarai, K.P., Shamseldin, A.Y., 2005. Assessing the performance of eight real-time updating models and procedures for the Brosna River. Hydrol. Earth Syst. Sci., 9(4): 394-411. https://doi.org/10.5194/hess-9-394-2005

Guinot, V., Savean, M., Jourde, H., Neppel, L., 2015. Conceptual rainfall-runoff model with a two-parameter, infinite characteristic time transfer function. Hydrol. Processes, 29(22): 4756-4778. https://doi.org/10.1002/hyp.10523

Hadadin, N.A., Tarawneh, Z.S., 2007. Environmental issues in Jordan, solutions and recommendations. Am. J. Environ. Sci., 3(1): 30-36. https://doi.org/10.3844/ajessp.2007.30.36

Hsu, K.L., Gupta, H.V., Sorooshian, S., 1995. Artificial Neural-Network Modeling of the Rainfall-Runoff Process. Water Resour. Res., 31(10): 2517-2530. https://doi.org/10.1029/95WR01955

Idczak, D., Kamocki, R., 2011. On the existence and uniqueness and formula for the sollution of R-L fractional Cauchy problem in R^n. Fract Calc Appl Anal, 14(4): 538-553. https://doi.org/10.2478/s13540-011-0033-5

Jarad, F., Abdeljawad, T., 2018. A modified Laplace transform for certain generalized fractional operators. Results in Nonlinear Analysis, 1(2): 88-98. https://doi.org/10.3934/dcdss.2020039

Kamocki, R., 2014a. On the existence of optimal solutions to fractional optimal control problems. Appl. Math. Comput., 235: 94-104. https://doi.org/10.1016/j.amc.2014.02.086

Kamocki, R., 2014b. Pontryagin maximum principle for fractional ordinary optimal control problems. Math Method Appl Sci, 37(11): 1668-1686. https://doi.org/10.1002/mma.2928

Kamocki, R., Majewski, M., 2015. Fractional linear control systems with Caputo derivative and their optimization. Optim Contr Appl Met, 36(6): 953-967. https://doi.org/10.1002/oca.2150

Karlsson, M., Yakowitz, S., 1987. Rainfall-Runoff Forecasting Methods, Old and New. Stoch. Hydrol. Hydraul., 1(4): 303-318. https://doi.org/10.1007/Bf01543102

Lohani, A.K., Goel, N.K., Bhatia, K.K.S., 2011. Comparative study of neural network, fuzzy logic and linear transfer function techniques in daily rainfall-runoff modelling under different input domains. Hydrol. Processes, 25(2): 175-193. https://doi.org/10.1002/hyp.7831

Oldham, K.B., Spanier, J., 1974. The Fractional Calculus. Academic Press, Inc., 234 pp.

Osman, Y., Al-Ansari, N., Abdellatif, M., 2019. Climate change model as a decision support tool for water resources management in northern Iraq: a case study of Greater Zab River. J. Water Clim. Change, 10(1): 197-209. https://doi.org/10.2166/wcc.2017.083

Richardson, C.W., Wright, D.A., 1984. WGEN: A model for generating daily weather variables. US Department of Agriculture, Agricultural Research Service Washington, DC, USA.

Rosmann, T., Dominguez, E., 2018. A Fokker-Planck-Kolmogorov equation-based inverse modelling approach for hydrological systems applied to extreme value analysis. J. Hydroinform., 20(6): 1296-1309. https://doi.org/10.2166/hydro.2017.079

Sharifi, E. et al., 2015. Design and construction of a hydraulic structure for rainwater harvesting in arid environment. Proceedings of the 36th IAHR World Congress: 3375-3386.

Sharifi, E., Unami, K., Yangyuoru, M., Fujihara, M., 2016. Verifying optimality of rainfed agriculture using a stochastic model for drought occurrence. Stoch. Environ. Res. Risk Assess., 30(5): 1503-1514. https://doi.org/10.1007/s00477-015-1129-y

Spolia, S.K., Chander, S., Oconnor, K.M., 1980. An auto-correlation approach for parameter-estimation of fractional order equal-root autoregressive models using hypergeometric functions. J. Hydrol., 47(1-2): 1-17. https://doi.org/10.1016/0022-1694(80)90044-X

Tarawneh, Q., Kadıoğlu, M., 2003. An analysis of precipitation climatology in Jordan. Theor. Appl. Climatol., 74(1-2): 123-136. https://doi.org/10.1007/s00704-002-0705-5

Unami, K., Kawachi, T., 2005. Systematic assessment of flood mitigation in a tank irrigated paddy fields area. Paddy Water Environ., 3(4): 191-199. https://doi.org/10.1007/s10333-005-0022-6

Unami, K., Mohawesh, O., 2018. A unique value function for an optimal control problem of irrigation water intake from a reservoir harvesting flash floods. Stoch. Environ. Res. Risk Assess., 32(11): 3169-3182. https://doi.org/10.1007/s00477-018-1527-z

Unami, K., Mohawesh, O., Fadhil, R.M., 2019. Time periodic optimal policy for operation of a water storage tank using the dynamic programming approach. Appl. Math. Comput., 353: 418-431. https://doi.org/10.1016/j.amc.2019.02.005

Unami, K., Mohawesh, O., Fujihara, M., 2020. Prototype and model of solar driven desalination plant in arid environment. Therm. Sci., 24(2): 903-914. https://doi.org/10.2298/Tsci180604097u

Unami, K., Mohawesh, O., Sharifi, E., Takeuchi, J., Fujihara, M., 2015. Stochastic modelling and control of rainwater harvesting systems for irrigation during dry spells. J. Clean. Prod., 88: 185-195. https://doi.org/10.1016/j.jclepro.2014.03.100

Van Afferden, M. et al., 2010. A step towards decentralized wastewater management in the Lower Jordan Rift Valley. Water Sci. Technol., 61(12): 3117-3128. https://doi.org/10.2166/wst.2010.234

Vedula, S., Mujumdar, P.P., 2005. Water resources systems. Tata McGraw-Hill Education, New

Delhi.

Figure 1

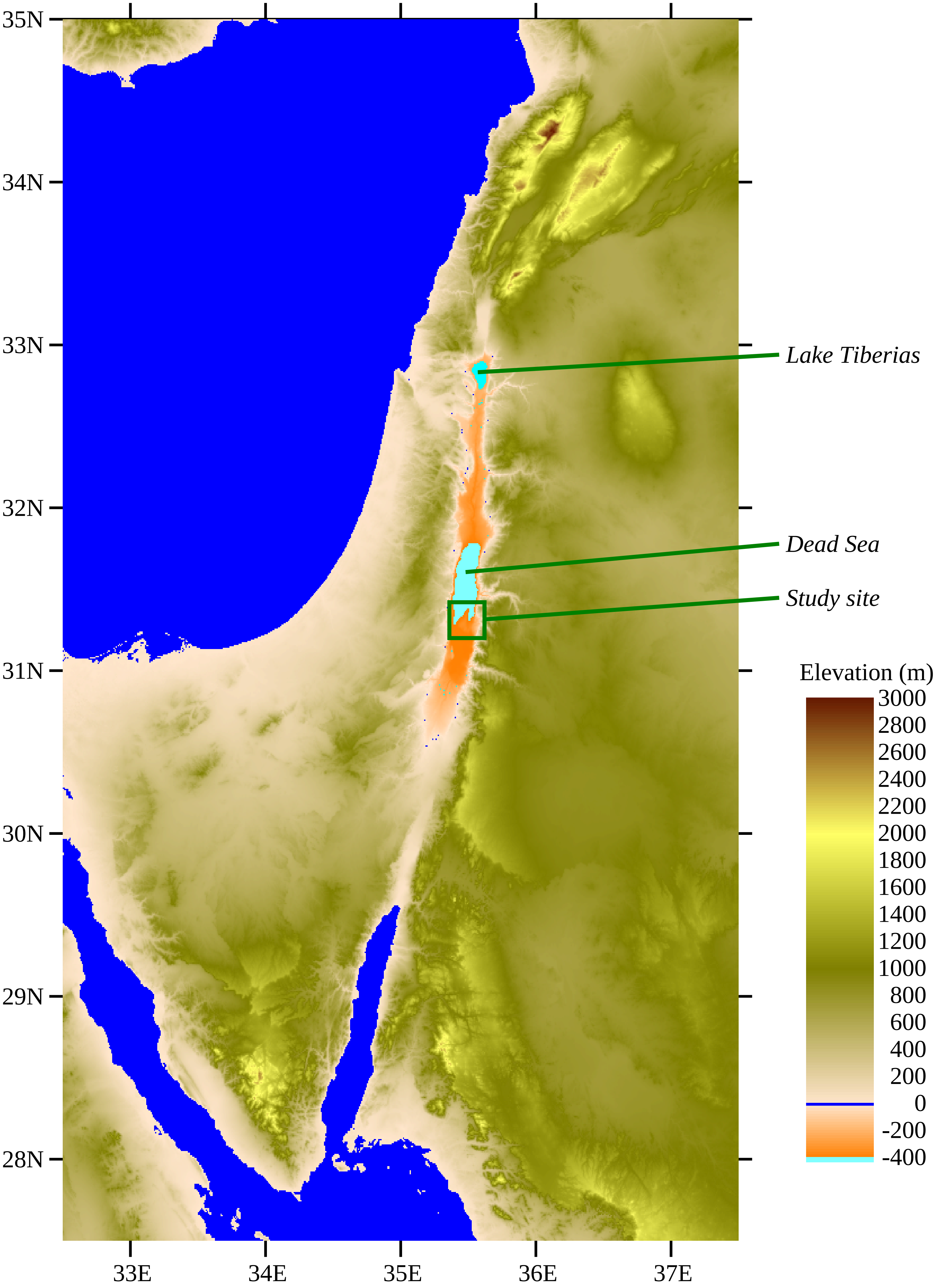
35N
34N
33N
32N
31N
30N
29N
28N
33E
34E
35E
36E
37E
Lake Tiberias
Dead Sea
Study site
Elevation (m)
3000
2800
2600
2400
2200
2000
1800
1600
1400
1200
1000
800
600
400
200
0
-200
-400

Figure 2

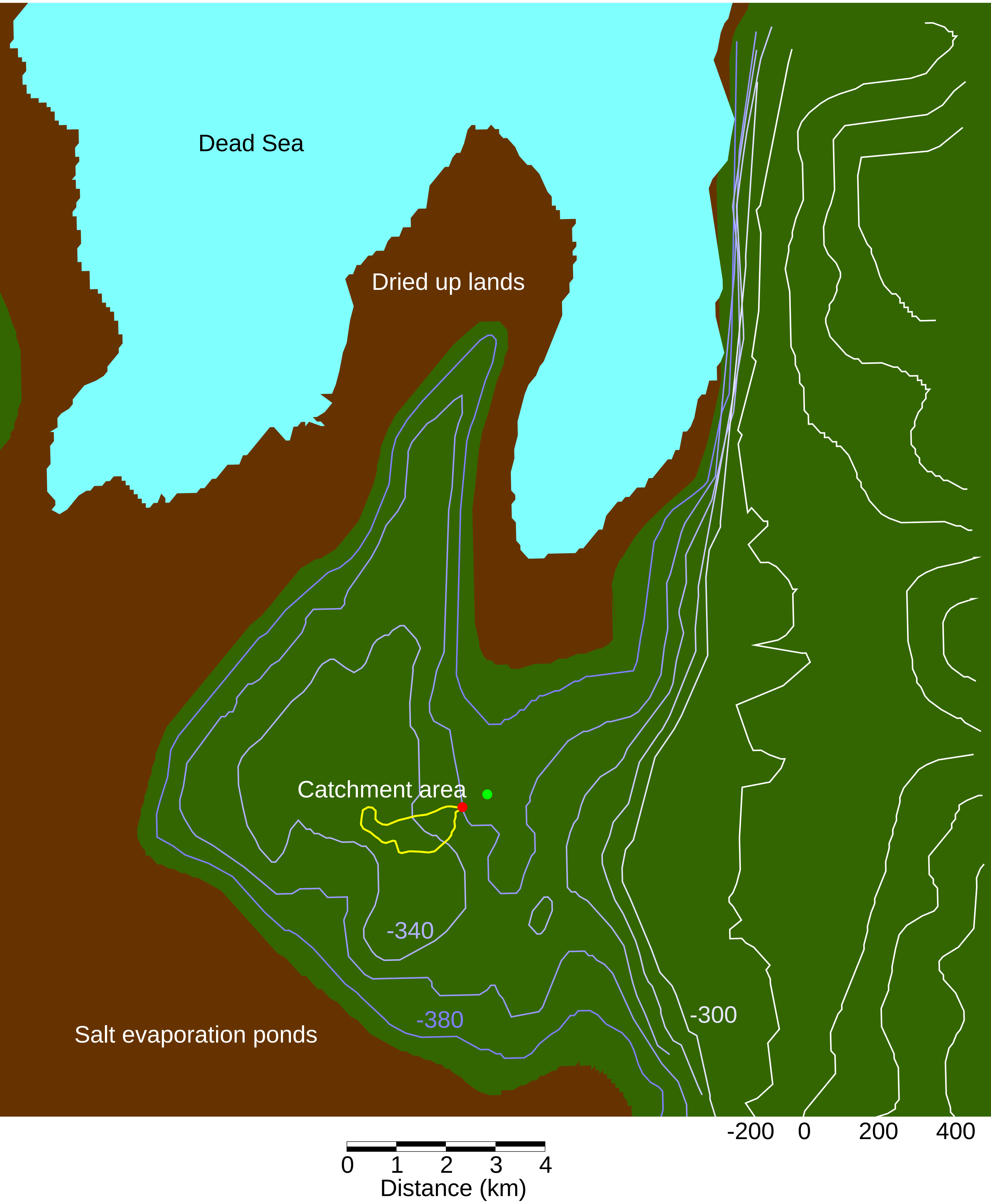
Dead Sea
Dried up lands
Catchment area
-340
-380
-300
Salt evaporation ponds
-200
0
200
400
0
1
2
3
4
Distance (km)

Figure 3
Click here to download high resolution image

Figure 4

Click here to download high resolution image

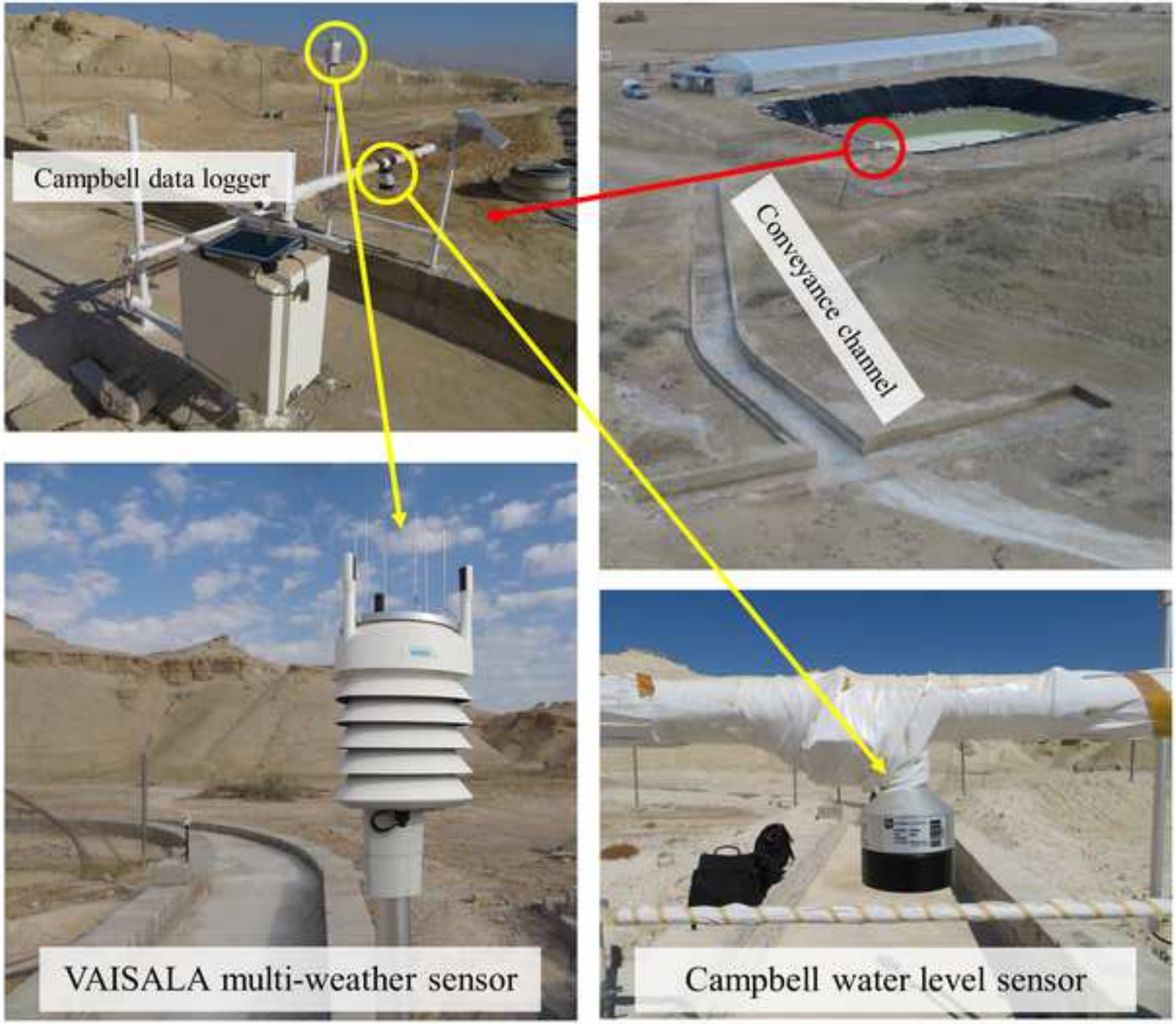

Figure 5

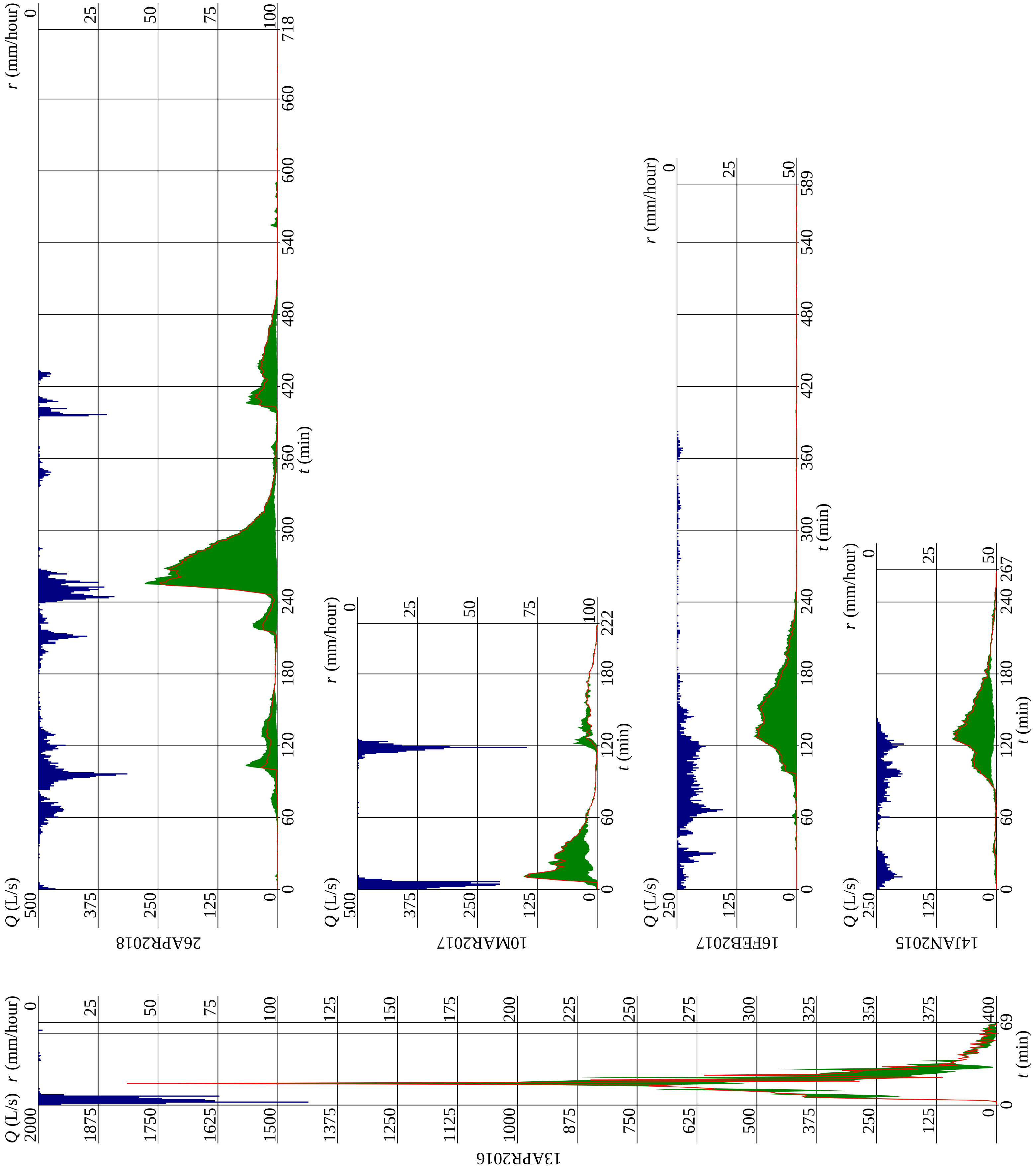

26APR2018
10MAR2017
16FEB2017
14JAN2015
13APR2016
Q (L/s)
r (mm/hour)
t (min)

Figure 6

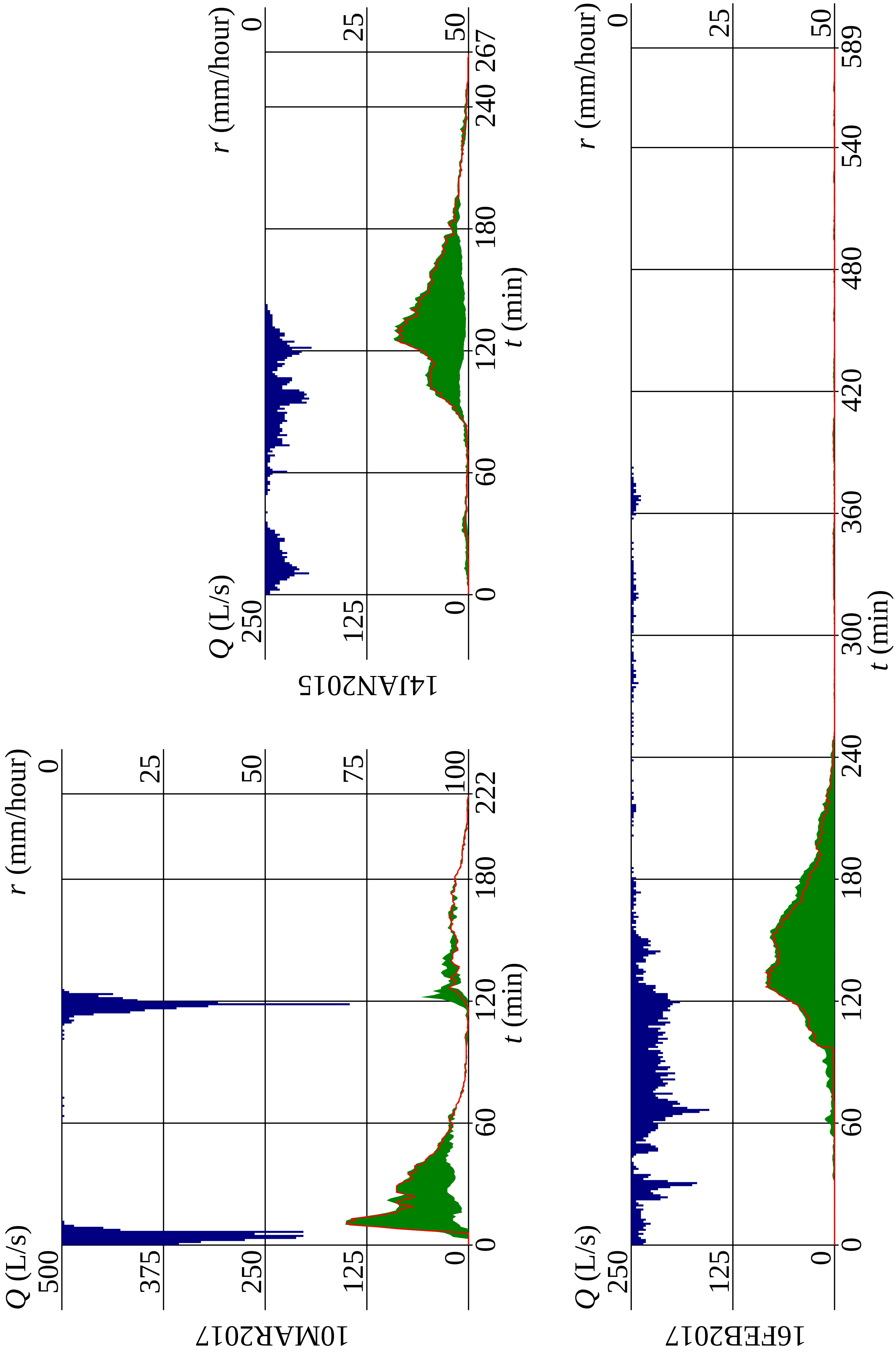

Figure 7

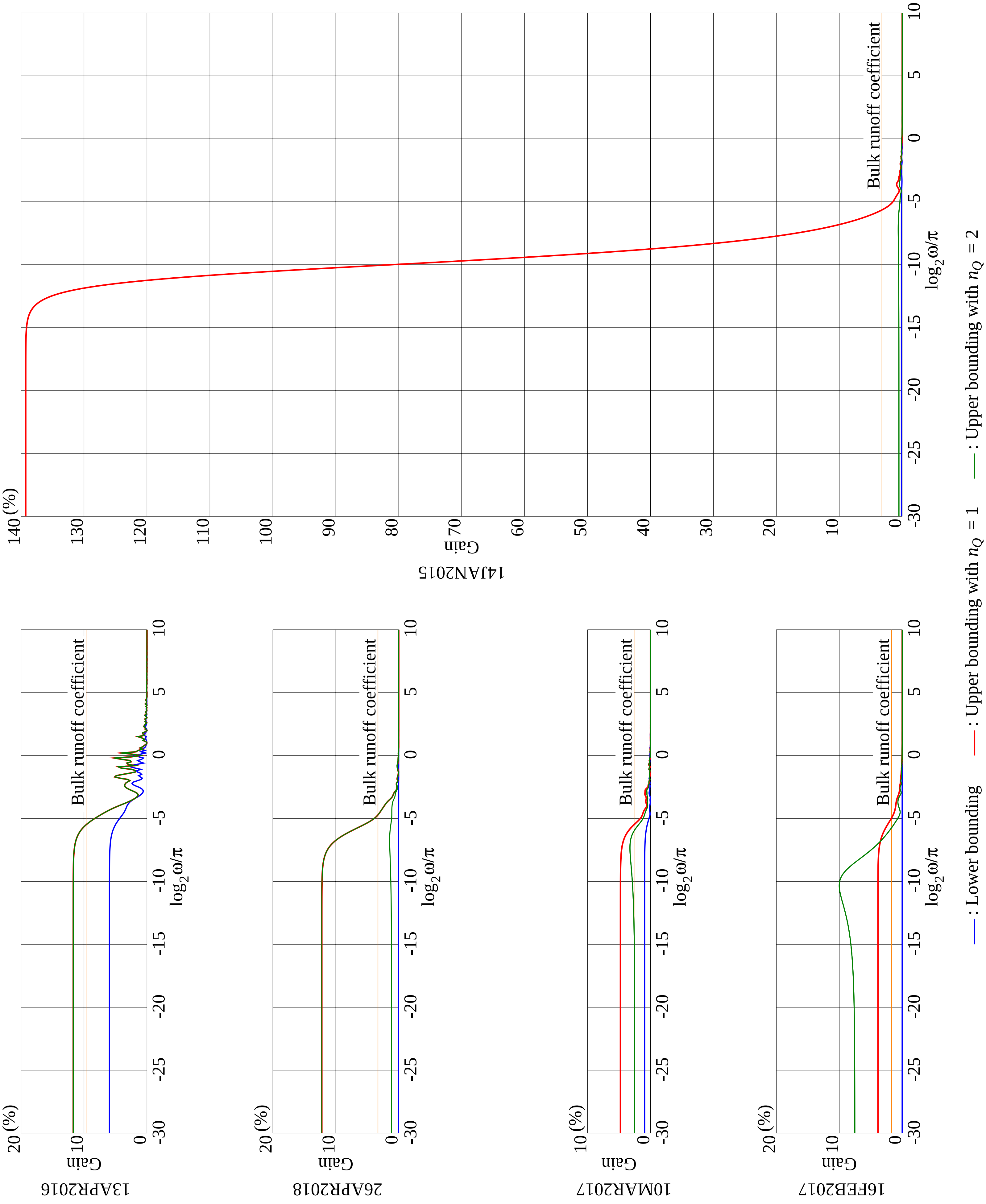
13APR2016
26APR2018
10MAR2017
16FEB2017
14JAN2015
Gain
(%)
Bulk runoff coefficient
$\log_2\omega/\pi$
: Lower bounding
: Upper bounding with $n_Q = 1$
: Upper bounding with $n_Q = 2$

Figure 8

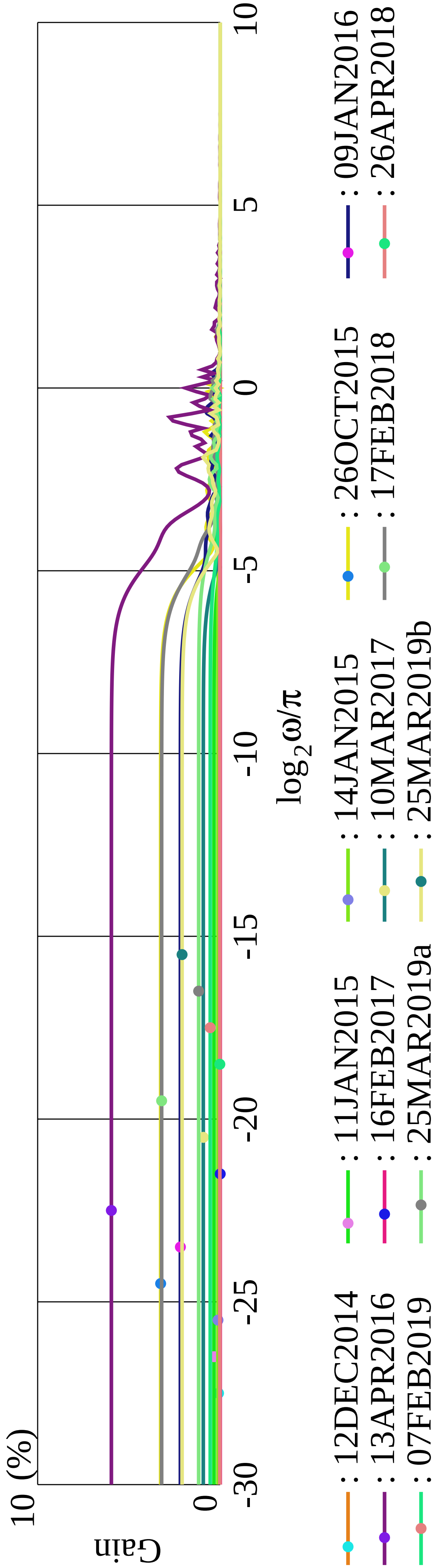

Gain
10 (%)
0
-30
-25
-20
-15
-10
-5
0
5
10
$\log_2 \omega/\pi$
: 12DEC2014
: 11JAN2015
: 14JAN2015
: 26OCT2015
: 09JAN2016
: 13APR2016
: 16FEB2017
: 10MAR2017
: 17FEB2018
: 26APR2018
: 07FEB2019
: 25MAR2019a
: 25MAR2019b

Figure 9

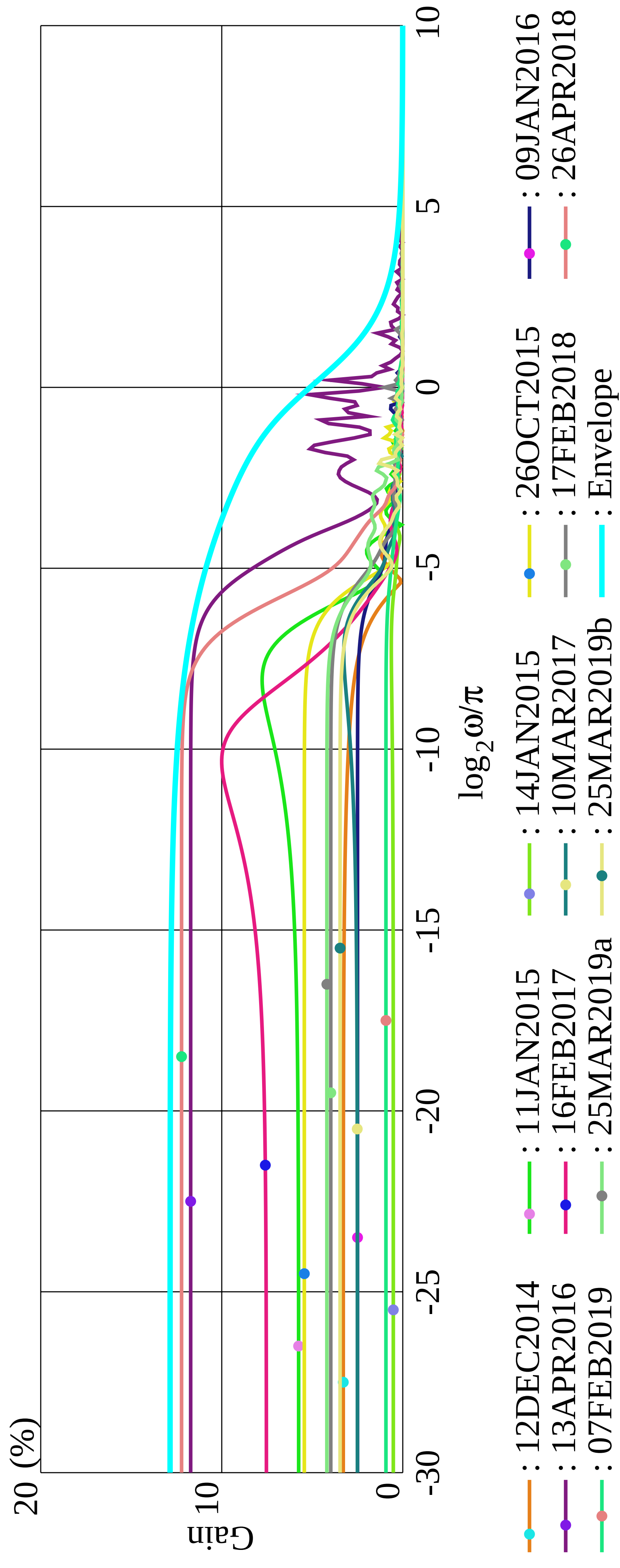
Gain
(%)
20
10
0
-30
-25
-20
-15
-10
-5
0
5
10
log2ω/π
: 12DEC2014
: 11JAN2015
: 14JAN2015
: 26OCT2015
: 09JAN2016
: 13APR2016
: 16FEB2017
: 10MAR2017
: 17FEB2018
: 26APR2018
: 07FEB2019
: 25MAR2019a
: 25MAR2019b
: Envelope

Figure 10

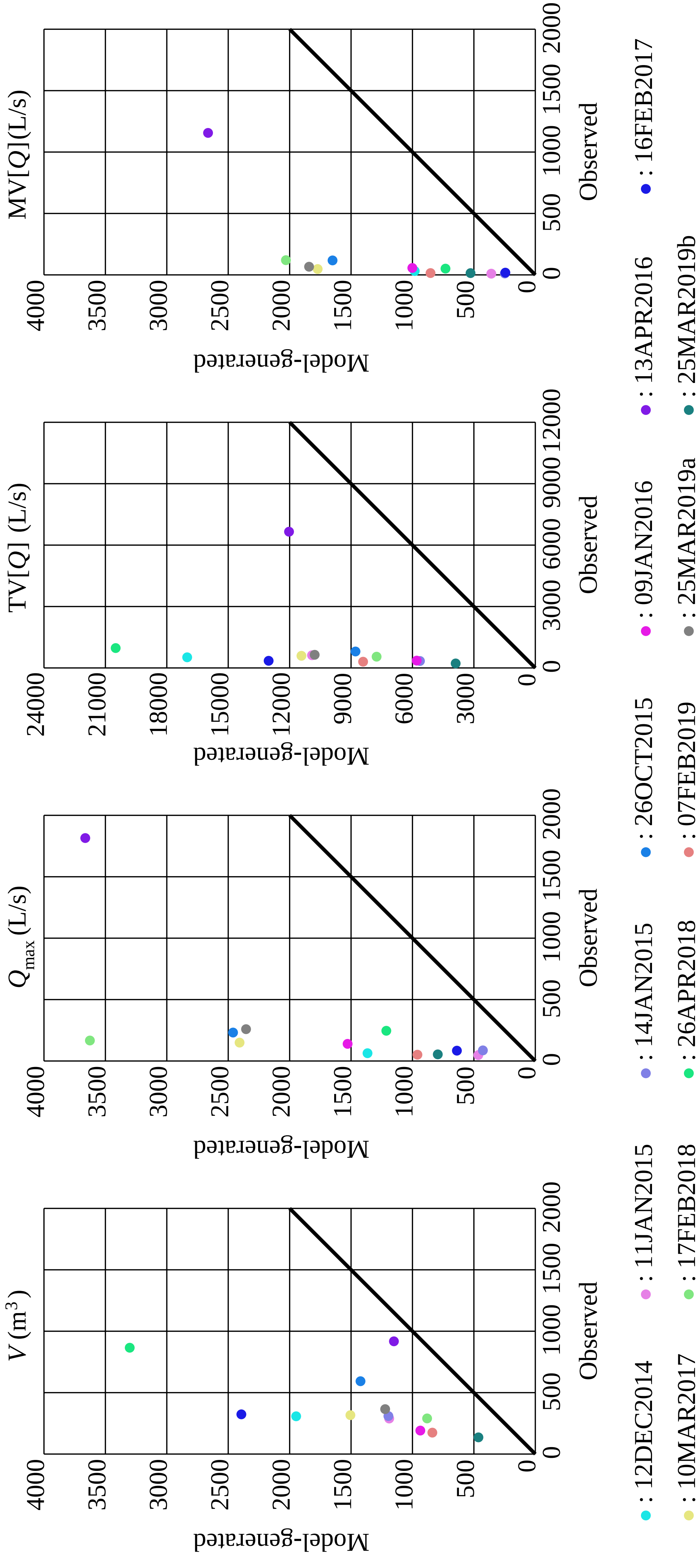

V (m3)
Qmax (L/s)
TV[Q] (L/s)
MV[Q](L/s)
Model-generated
Observed
: 12DEC2014
: 11JAN2015
: 14JAN2015
: 26OCT2015
: 09JAN2016
: 13APR2016
: 16FEB2017
: 10MAR2017
: 17FEB2018
: 26APR2018
: 07FEB2019
: 25MAR2019a
: 25MAR2019b

Table 1
Click here to download Table: MazrahHYDROL_Table1.docx

Table 1: Basic meteorological data of rainfall depth *D* (mm) and air temperature *T* (℃) obtained at the study site for each water year.

		AUG	SEP	OCT	NOV	DEC	JAN	FEB	MAR	APR	MAY	JUN	JUL	Annual
D (mm)	2014-2015			6.58	10.51	21.11	29.35	21.80	4.30	10.59	0.00	0.00	0.00	104.71
	2015-2016	0.00	1.09	27.47	2.82	6.99	13.09	26.18	10.35	21.81	0.02	0.00	0.16	109.98
	2016-2017	0.00	0.00	3.79	0.47	11.41	4.63	26.27	14.50	1.65	0.37	0.30	0.00	63.39
	2017-2018	0.03	0.04	0.03	1.22	3.65	19.19	25.98	0.17	23.79	4.60	0.89	0.06	79.65
	2018-2019	0.06	0.18	3.60	9.70	1.20	1.53	15.07	29.21	5.8	0.00	0.00	0.00	66.35
T (℃)	Maximum	46.3	42.7	39.4	33.7	27.7	25.6	30.8	35.3	42.3	45.0	43.8	47.1	47.1
	Mean	34.4	32.5	28.3	22.7	17.8	15.9	18.0	21.6	25.4	29.6	32.2	34.3	26.1
	Minimum	25.9	21.6	17.4	9.1	6.4	4.2	4.5	10.4	12.0	18.3	21.2	23.6	4.2

Table 2

Click here to download Table: MazrahHYDROL-R1_Table2.docx

Table 2: Observed rainfall-runoff events with total runoff volume more than 100 m^3.

Event ID	Start	End	N	D^o (mm)	D^a (mm)	V (m^3)	Q_{max} (L/s)	C (%)
12DEC2014	19:15	04:38+	564	13.81	12.0	307.49	63	1.99
11JAN2015	01:15	08:32	390	8.52	10.5	289.23	48	3.03
14JAN2015	22:52	03:18+	267	8.59	8.4	309.39	86	3.22
26OCT2015	08:08	10:42	155	10.28	7.8	593.02	232	5.15
09JAN2016	02:39	04:36	118	6.79	2.7	191.19	140	2.51
13APR2016	15:32	16:40	69	8.47	3.4	917.84	1815	9.68
16FEB2017	10:46	20:34	589	16.97	10.4	323.32	84	1.70
10MAR2017	21:33	01:14+	222	10.85	5.4	316.78	150	2.61
17FEB2018	07:48	09:53	126	6.38	4.4	290.12	167	4.06
26APR2018	16:58	04:55+	718	23.40	14.7	865.60	246	3.30
07FEB2019	05:41	11:27	347	6.00	6.0	174.38	51	2.59
25MAR2019a	01:30	03:58	149	8.86	6.0	365.69	259	3.69
25MAR2019b	09:59	12:03	125	3.36	3.6	135.90	54	3.61

Table 3
Click here to download Table: MazrahHYDROL_Table3.docx

Table 3: Identified parameters of upper bounding models.

Event ID	$n_Q = 1$			$n_Q = 2$				
	$x_{n_r}^U$	a_0^U	a_1^U	$x_{n_r}^U$	$x_{n_r+1}^U$	a_0^U	$a_{1/2}^U$	a_1^U
12DEC2014	0.573552	0.42645	0.57355	0.296595	0.326290	0.19810	0.44871	0.59115
11JAN2015	0.764036	0.23596	0.76404	0.636273	0.152438	-0.17274	0.96261	0.17310
14JAN2015	1.002204	-0.00220	1.00220	0.978113	0.022239	-0.59070	1.47977	-0.15810
26OCT2015	0.567514	0.43249	0.56751	0.567514	0.000000	0.08996	0.85858	-0.11754
09JAN2016	0.000000	1.00000	0.00000	0.000000	0.000000	1.00000	0.00000	0.00000
13APR2016	0.000000	1.00000	0.00000	0.000000	0.000000	1.00000	0.00000	0.00000
16FEB2017	0.937808	0.06219	0.93781	0.325317	0.520431	-0.04209	0.49217	0.97349
10MAR2017	0.821041	0.17896	0.82104	0.736143	0.121345	-0.30179	1.11370	0.09023
17FEB2018	0.000000	1.00000	0.00000	0.000000	0.000000	1.00000	0.00000	0.00000
26APR2018	0.951410	0.04859	0.95141	0.951410	0.000000	-0.52564	1.43937	-0.19704
07FEB2019	0.000000	1.00000	0.00000	0.000000	0.000000	1.00000	0.00000	0.00000
25MAR2019a	0.584142	0.41586	0.58414	0.584142	0.000000	0.06330	0.88374	-0.12098
25MAR2019b	0.408625	0.59138	0.40863	0.408625	0.000000	0.34475	0.61820	-0.08463

Table 4
Click here to download Table: MazrahHYDROL-R1_Table4.docx

Table 4: Performance indices of the upper bounding linear ARX models.

	$n_Q = 1$, upper bounding					$n_Q = 2$, upper bounding				
Event ID	E_1	E_2	E_∞	E_{TV}	NSE	E_1	E_2	E_∞	E_{TV}	NSE
12DEC2014	1.565	7.898	23.134	722.093	0.957	1.549	8.670	26.458	631.920	0.953
11JAN2015	3.463	18.105	15.502	962.179	0.840	3.416	17.472	15.508	912.356	0.845
14JAN2015	2.770	13.440	12.278	552.868	0.976	2.769	13.346	12.055	545.175	0.976
26OCT2015	4.691	151.583	72.812	865.296	0.973	4.691	151.583	72.812	865.296	0.973
09JAN2016	1.432	28.304	37.157	210.674	0.975	1.432	28.304	37.157	210.674	0.975
13APR2016	47.068	19197.300	757.115	5547.450	0.798	47.068	19197.300	757.115	5547.450	0.798
16FEB2017	2.284	13.264	15.589	695.178	0.967	2.236	13.139	14.877	527.160	0.968
10MAR2017	4.310	66.889	41.852	641.710	0.928	4.201	63.070	49.056	632.411	0.932
17FEB2018	1.712	81.778	78.933	235.691	0.969	1.712	81.778	78.933	235.691	0.969
26APR2018	4.452	62.171	43.093	1516.090	0.969	4.452	62.171	43.093	1516.090	0.969
07FEB2019	2.545	19.545	30.068	628.764	0.821	2.545	19.545	30.068	628.764	0.821
25MAR2019a	3.780	72.605	50.390	352.085	0.977	3.780	72.605	50.390	352.085	0.977
25MAR2019b	1.517	8.126	13.540	196.720	0.969	1.517	8.126	13.540	196.720	0.969

Table 5
Click here to download Table: MazrahHYDROL-R1_Table5.docx

Table 5: Performance indices of the lower bounding linear ARX models and changes in performance indices of the upper bounding linear ARX models by increasing n_Q from 1 to 2.

	$n_Q=1$ and $n_Q=2$, lower bounding					Change by $n_Q=2$, upper bounding				
Event ID	E_1	E_2	E_∞	E_{TV}	NSE	E_1	E_2	E_∞	E_{TV}	NSE
12DEC2014	5.613	166.217	60.900	610.677	0.098	-0.016	0.772	3.324	-90.173	-0.004189
11JAN2015	9.775	194.248	43.210	687.923	-0.721	-0.047	-0.633	0.006	-49.823	0.005604
14JAN2015	14.520	704.442	83.139	363.182	-0.271	0.000	-0.094	-0.223	-7.693	0.000169
26OCT2015	17.469	2934.520	221.547	806.570	0.469	0.000	0.000	0.000	0.000	0.000000
09JAN2016	2.117	50.560	43.919	306.518	0.956	0.000	0.000	0.000	0.000	0.000000
13APR2016	85.599	41845.700	1290.490	6212.390	0.559	0.000	0.000	0.000	0.000	0.000000
16FEB2017	9.122	486.232	84.053	350.208	-0.202	-0.048	-0.125	-0.712	-168.018	0.000309
10MAR2017	13.013	907.619	135.284	590.776	0.026	-0.109	-3.819	7.204	-9.299	0.004098
17FEB2018	5.742	682.348	159.947	412.262	0.740	0.000	0.000	0.000	0.000	0.000000
26APR2018	18.554	2306.780	244.600	1042.360	-0.154	0.000	0.000	0.000	0.000	0.000000
07FEB2019	5.349	124.078	47.743	381.591	-0.137	0.000	0.000	0.000	0.000	0.000000
25MAR2019a	25.462	3662.110	254.667	763.074	-0.163	0.000	0.000	0.000	0.000	0.000000
25MAR2019b	4.905	163.235	48.134	217.040	0.381	0.000	0.000	0.000	0.000	0.000000